Individual and collective manipulation of multifunctional bimodal droplets in three dimensions

Sun, Mengmeng; Sun, Bonan; Park, Myungjin; Yang, Shihao; Wu, Yingdan; Zhang, Mingchao; Kang, Wenbin; Yoon, Jungwon; Zhang, Li; Sitti, Metin

Published in:
Science Advances

Published: 01/07/2024

Document Version:
Final Published version, also known as Publisher's PDF, Publisher's Final version or Version of Record

Published version (DOI):
10.1126/sciadv.adp1439

Publication details:
Sun, M., Sun, B., Park, M., Yang, S., Wu, Y., Zhang, M., Kang, W., Yoon, J., Zhang, L., & Sitti, M. (2024). Individual and collective manipulation of multifunctional bimodal droplets in three dimensions. *Science Advances*, *10*(29), Article eadp1439. https://doi.org/10.1126/sciadv.adp1439

APPLIED SCIENCES AND ENGINEERING

Individual and collective manipulation of multifunctional bimodal droplets in three dimensions

Mengmeng Sun[1]†, Bonan Sun[2]†, Myungjin Park[1,3]†, Shihao Yang[2], Yingdan Wu[1], Mingchao Zhang[1], Wenbin Kang[1], Jungwon Yoon[3], Li Zhang[2]*, Metin Sitti[1,4]*

Spatiotemporally controllable droplet manipulation is vital across numerous applications, particularly in miniature droplet robots known for their exceptional deformability. Despite notable advancements, current droplet control methods are predominantly limited to two-dimensional (2D) deformation and motion of an individual droplet, with minimal exploration of 3D manipulation and collective droplet behaviors. Here, we introduce a bimodal actuation strategy, merging magnetic and optical fields, for remote and programmable 3D guidance of individual ferrofluidic droplets and droplet collectives. The magnetic field induces a magnetic dipole force, prompting the formation of droplet collectives. Simultaneously, the optical field triggers isothermal changes in interfacial tension through Marangoni flows, enhancing buoyancy and facilitating 3D movements of individual and collective droplets. Moreover, these droplets can function autonomously as soft robots, capable of transporting objects. Alternatively, when combined with a hydrogel shell, they assemble into jellyfish-like robots, driven by sunlight. These findings present an efficient strategy for droplet manipulation, broadening the capabilities of droplet-based robotics.

INTRODUCTION

Controlling droplets is crucial in various practical applications, spanning biomedical fields (*1*, *2*), chemical reactions (*3*), thermal regulation (*4*), water harvesting (*5*), and electronics (*6*). Various external stimuli, such as magnetic (*7*, *8*), electrical (*9*, *10*), optical (*11*, *12*), and ultrasound (*13*, *14*) are used to enhance the flexibility and precision of droplet manipulation. Thanks to substantial technological advancements in the past decade, we can now transport, merge, disperse, trap, and sort individual droplets at remarkably high throughput (*15*–*17*). The fluidity of droplets also offers vast design possibilities for miniature soft robots (*18*, *19*), promising breakthroughs in biomedical applications (*20*–*22*), particularly in accessing hard-to-reach sites of the human body. To address the limitations of conventional soft robots, particularly those based on magnetic elastomers (*23*–*25*), recent research has focused on droplet-based robots with enhanced deformation capabilities, such as liquid metal robots (*26*–*30*) and ferrofluid robots (*31*–*34*). For instance, a two-dimensional (2D) ferrobotic system using ferrofluid facilitates the measurement of active-matrix metallopeptidases (a cancer malignancy and inflammation biomarker) in human plasma and the detection of the SARS-CoV-2 virus in clinical samples (*35*, *36*). Another ferrofluid robotic system, using a 2D electromagnetic array, enables targeted drug delivery and delicate object manipulation (*32*). Magnetic slime robots, using non-Newtonian fluids, demonstrate versatility and on-the-fly reconfiguration capabilities (*37*). Liquid droplet–based robots with superior deformation capabilities can undergo extreme transformations, such as splitting and fusion, leading to increased flexibility and scalability (*38*).

However, current research primarily concentrates on the deformation and manipulation of individual droplets within a 2D plane (*39*–*41*). This focus not only constrains the potential application scenarios of droplets but also restricts the functionality and operational capabilities of droplet-based miniature soft robots (*28*, *32*, *42*, *43*). While 3D manipulation of droplets can be achieved using external tools such as magnetic cilia or magnetic tweezers (*44*, *45*), their passive motion dependent on such tools hinders adaptability to unstructured environments, thereby limiting their utility across various potential applications. Consequently, achieving 3D manipulation and active deformation of individual droplets stands as a crucial challenge in this field. Moreover, there has been limited exploration into the interactions among multiple droplets and their self-organizing behaviors (*15*, *31*), particularly concerning in situ manipulation and reconfiguration of multiple droplet collectives. This aspect holds practical significance as liquid droplets seldom exist in isolation but rather in clusters. Effectively regulating droplet collectives can enhance task efficiency of droplet-based robots and substantially augment the versatility of miniature robots.

In our study, we introduce a bimodal strategy for 3D manipulation of both individual droplets and droplet collectives. This strategy relies on two external fields: magnetic and light fields. Magnetic fields serve to modulate the morphology and orientation of individual droplets, facilitating their division into multiple sub-droplets and subsequent assembly into droplet collectives. By adjusting the parameters of the external magnetic field, diverse patterns of droplet collectives emerge, ranging from chain-like and layer-stacked structures to dispersed columnar formations. Furthermore, the application of light fields induces Marangoni flows within the droplets, and the droplets expand in volume, causing them to acquire upward lift. Through precise parameter adjustments of the light field, individual droplets can maneuver on a 2D plane, hover in 3D space, navigate directionally, and even traverse continuous obstacles. Notably, the light field not only influences the morphology of droplet collectives, enabling the assembly of dispersed columnar structures into higher pyramidal formations, but also grants them the capability of 3D

[1]Physical Intelligence Department, Max Planck Institute for Intelligent Systems, 70569 Stuttgart, Germany. [2]Department of Mechanical and Automation Engineering, The Chinese University of Hong Kong, Hong Kong SAR, China. [3]School of Integrated Technology, Gwangju Institute of Science and Technology, Gwangju, Korea. [4]School of Medicine and College of Engineering, Koç University, 34450 Istanbul, Turkey.
*Corresponding author. Email: sitti@is.mpg.de (M.S.); lizhang@cuhk.edu.hk (L.Z.)
†These authors contributed equally to this work.

movement and hovering. Illustrated in Fig. 1A, the control principle of droplets elucidates their operational versatility. Figure 1B showcases various functionalities of droplets, including traversing complex obstacles, self-assembling into collectives for levitation tasks, or acting as actuators in jellyfish-like structures, thereby achieving sunlight-driven locomotion. Compared to conventional ferrofluid droplets controlled solely by magnetic fields (*31*–*36*, *46*–*48*), the utilization of coupling fields in magnetic droplets yields more intricate motion patterns and collective behaviors. This advancement substantially broadens the potential applications of droplet-based robots within the realm of miniature soft robotics.

RESULTS

Governing mechanism of 3D locomotion of individual ferrofluidic droplets

The coprecipitation method is used for synthesizing Fe_3O_4 nanoparticles coated with oleic acid (*49*–*51*). Subsequently, these nanoparticles are incorporated into mineral oil, resulting in the formation of an oil-based ferrofluid (please refer to Materials and Methods and fig. S1 for detailed procedures). Fe_3O_4 nanoparticles, coated with oleic acid, are uniformly dispersed in the mineral oil, exhibiting the capability to absorb near-infrared (NIR) light and convert it into heat energy via photothermal conversion. As depicted in fig. S2A, observations from an infrared camera reveal that upon directing an infrared laser at the surface of the ferrofluid from 10 cm, the surface temperature of the ferrofluid increases from room temperature (25°C) to 140°C in approximately 15 s. The magnitude of laser power influences the maximum temperature attained on the ferrofluid surface: At 3 W/cm^2, the surface temperature reaches 70°C, whereas at 15 W/cm^2, it escalates to 160°C (fig. S2, B and C). Snapshots captured by a high-speed camera depict that upon placing ferrofluid droplets in a water phase environment and subjecting them to laser irradiation (wavelength: 808 nm, intensity *I*: 24 W/cm^2, direction *D*: 90° vertical), the droplets exhibit vertical upward movement from the bottom (Fig. 2A and movie S1). Upon turning off the laser, the ferrofluid droplets promptly descend to the bottom. Volume expansion of the droplet under laser irradiation can be observed from

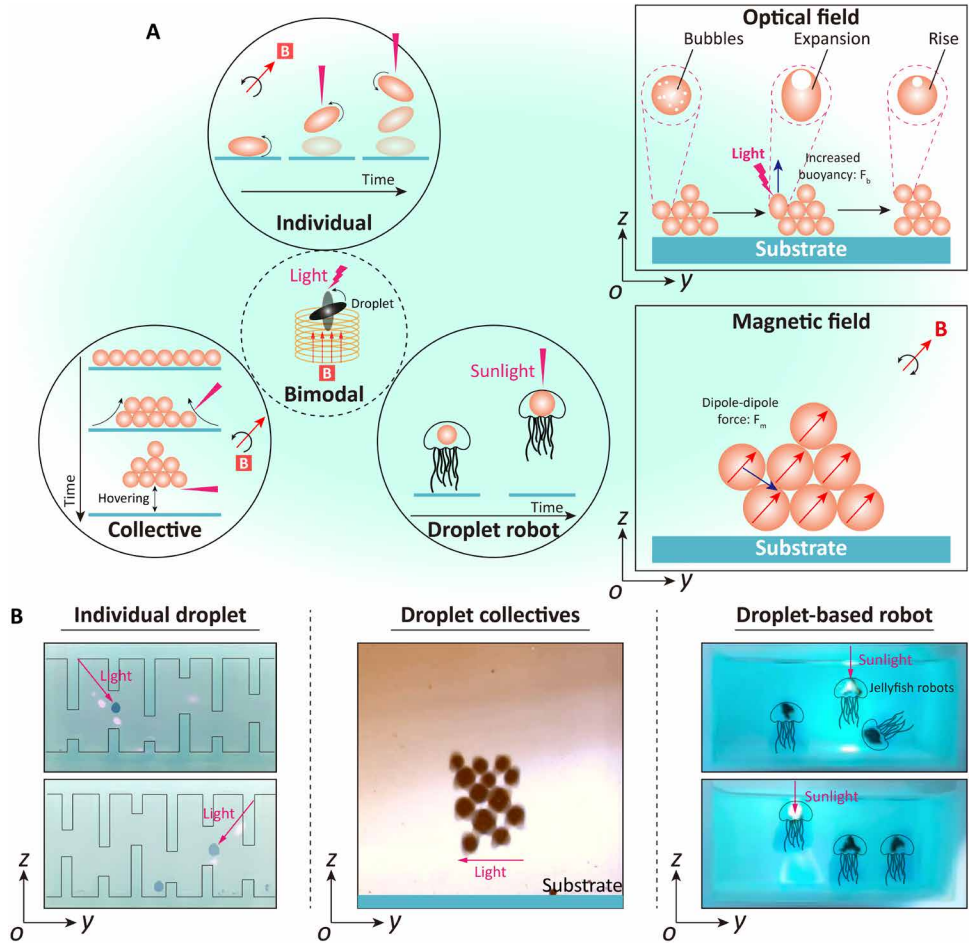

Fig. 1. Schematic and experiment snapshots showing the individual and assembling behavior of bimodal droplets. (**A**) Dual-responsible droplets perform 3D motion and selective control by coupling magnetic and optical fields. The optical field provides upward buoyancy for the droplets, and the magnetic field provides magnetic dipole force. Therefore, individual droplets can traverse complex 3D terrain like Flappy Bird, multiple droplets can be assembled into pyramidal structures and keep hovering or with hydrogel modules as jellyfish robots. (**B**) Snapshots showing that the droplets can climb over complex terrain or self-assemble into collectives and then remain suspended, or assemble with hydrogel shells to form jellyfish-like robots that move freely in the sunlight.

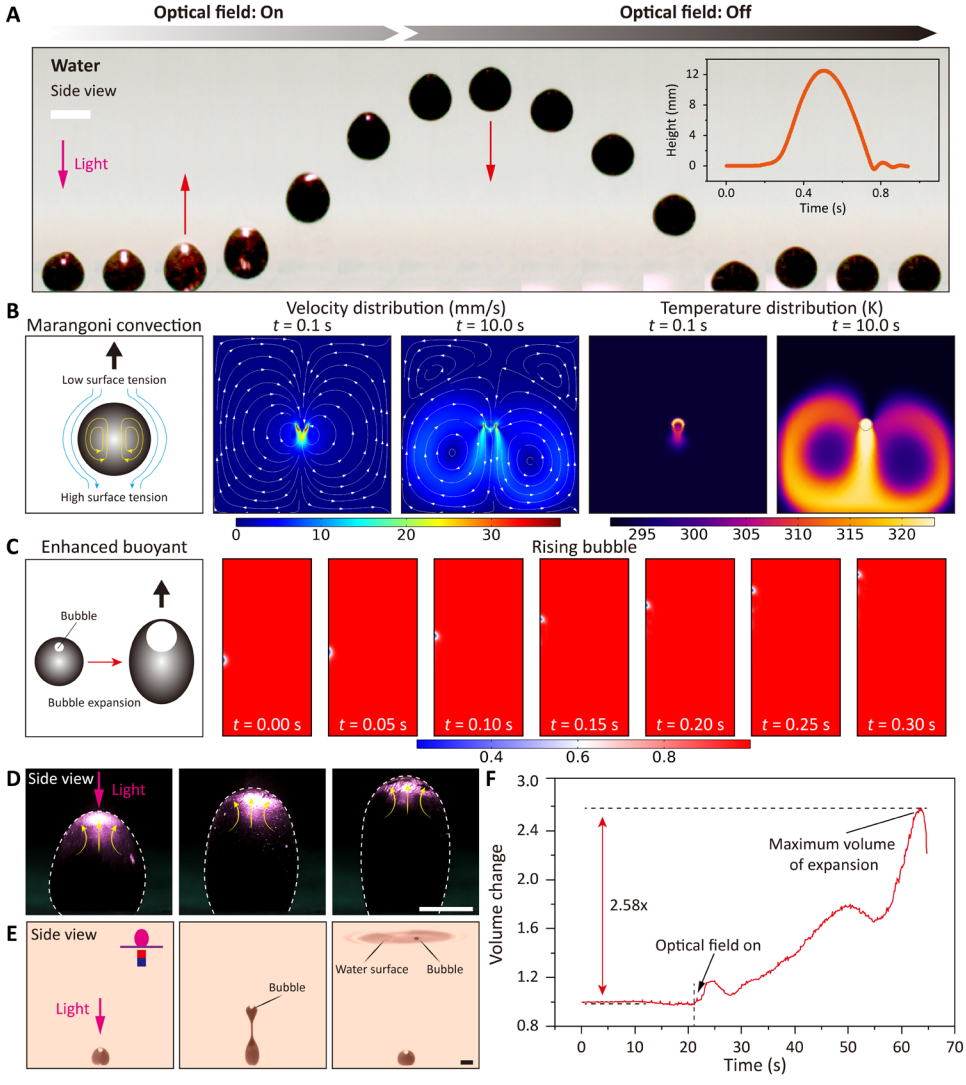

Fig. 2. 3D locomotion mechanism of the droplet. (**A**) High-speed camera snapshots show a droplet expanding and floating under NIR irradiation (optical field, $I = 24$ W/cm^2; $D = 90°$ vertical; magnetic field, off). The inset shows the height of the droplet versus time. (**B**) Illustration and simulation of a droplet moving by Marangoni flows. (**C**) Schematic and simulation showing thermal expansion of bubbles inside a droplet causing the droplet to rise. Optical field (optical field, $I = 24$ W/cm^2; $D = 90°$ vertical; magnetic field, permanent magnet with strength of 500 mT) induces the droplet to expand in volume (**D**), and, if a permanent magnet is used to lock the droplet to the substrate, bubbles can be observed to detach from the droplet and reach the surface of the water (**E**). (**F**) Optical field induced a 2.58-fold expansion in the volume of the droplets. Scale bars, 2 mm.

the snapshots obtained by the high-speed camera. When the optical field is deactivated, the droplet deformation ceases to expand and returns to its original approximate spherical state. The relationship between the vertical position height and irradiation time changes of the ferrofluid droplet demonstrates the exceptional responsiveness of the droplet to laser irradiation. Specifically, upon laser activation, the ferrofluid droplets ascend from the base to a height of 12 mm within 0.5 s.

The working principle of NIR laser-induced droplet 3D locomotion involves two primary mechanisms. First, localized laser spot irradiation on the ferrofluid droplet leads to temperature elevation, resulting in uneven temperature distribution between the ferrofluid and water phases. This temperature differential triggers Marangoni flows, propelling the droplet upward. Second, the heat-induced expansion of tiny bubbles within the ferrofluid droplet causes an increase in volume, thereby enhancing buoyancy and facilitating upward movement (see more details in note S1). In both drive mechanisms, enhanced buoyancy dominates. We first analyze the uneven temperature-induced thermocapillary flow. Upon laser irradiation, the droplet's surface experiences a gradual decrease in temperature from top to bottom due to gradual laser power absorption along the light path. Consequently, Marangoni convection arises inside and outside the droplet. Conservation of momentum dictates that the droplet moves in the opposite direction of the external Marangoni flow, resulting in upward floating. COMSOL simulation (Fig. 2B) indicates that the maximum flow velocity of the Marangoni flow generated by the droplet is approximately 30 mm/s when a temperature difference of 30 K exists between the upper and lower

surfaces of the droplet. In addition, the expansion of bubbles within the droplet also contributes to its floating behavior. COMSOL simulation and experimental verification support these two mechanisms (Fig. 2C). A permanent magnet fixes the ferrofluid droplet on the substrate, and tracer particles added to its surface allow observation of the trajectory of the particles under laser irradiation. This observation confirms the presence of Marangoni convection inside the droplet (Fig. 2D and movie S2). Moreover, the expansion of the droplet's volume is visibly observed during this process. Continued laser irradiation leads to droplet expansion and eventual splitting into two droplets. One droplet, attracted to the permanent magnet, remains fixed to the substrate, while the other, containing bubbles, continues to float upward and bursts upon reaching the water surface (Fig. 2E and movie S2). Throughout the expansion process until splitting, the droplet's maximum volume change rate is recorded as 2.58 times, indicating a corresponding increase in buoyancy compared to its initial state (Fig. 2F).

Motion control of individual droplets

In addition to vertical upward floating motion, the light field enables hovering and translational motion of individual droplets in 3D space. We systematically study the influence of light intensity and droplet volume on the vertical movement of droplet. Our findings reveal that a light field intensity exceeding 36 W/cm^2 is required for upward motion of ferrofluid droplets of various volumes (fig. S3). In addition, we observe that light intensity dictates both the height and speed of droplet ascent, with stronger light fields resulting in higher and faster ascent rates (fig. S4). Furthermore, droplet size also plays a notable role, as larger droplets rise lower and slower under the same light field intensity (fig. S5). Notably, ambient temperature can affect the rate of droplet rise (fig. S6). Specifically, as the temperature increases from 5° to 45°C, the droplet rising speed gradually increases. However, beyond 45°C, the rise velocity decreases significantly. We attribute this phenomenon to the influence of ambient temperature on the heat dissipation process of the droplet, ultimately determining the temperature difference between the droplet and the environment, and thereby affecting its rise rate. As depicted in Fig. 3A and the corresponding schematic diagram in fig. S7A, irradiating the NIR laser horizontally from the side propels the droplet to continuously ascend. After 10 s, the droplet reaches the target position, and the height of the optical path is then set at 5.5 mm. Subsequently, the droplet consistently performs up-and-down floating motion near the set height, with the height difference between its upward and downward motion within the range of 0.5 mm (movie S3). Similarly, directing a NIR laser at an inclined angle to the ferrofluid droplet, approximately 30°, induces translational motion in 3D space, as demonstrated in Fig. 3B and the corresponding schematic diagram in fig. S7A. In this scenario, the ferrofluid droplet translates 10 mm at a height of 3.5 mm without contacting the substrate within 15 s (movie S3). 3D motion capability upon the droplets by the light field enables individual droplets to adapt to complex 3D environments effectively. For instance, a ferrofluid droplet monomer with 3D locomotion capability can navigate through maze environments filled with obstacles, akin to the game "Flappy Bird," as illustrated in fig. S7B. As shown in fig. S7C, two ferrofluid droplets initially positioned at opposite ends of a vertical maze at $t = 0$ s traverse the vertical obstacles over 183 s under the influence of the light field, eventually converging at the maze's center.

When both the magnetic field and the light field are simultaneously applied, the droplet's mode can be adjusted during 3D motion. As depicted in Fig. 3C, under a vertical static magnetic field (with a magnetic field strength B of 9 mT and an angle α of 90° between the magnetic field and the horizontal plane), the ferrofluid droplet adopts a vertical shuttle shape. Subsequently, when a vertical light field is applied, the droplet maintains this shuttle shape while rising vertically (movie S4). Alternatively, under a static magnetic field, altering the angle α to 0° or 45° results in the ferrofluid droplet maintaining a horizontal shuttle or an inclined shuttle shape, respectively, before ascending vertically (fig. S8 and movie S4). Furthermore, in addition to the static magnetic field, a dynamic magnetic field can also be used. As illustrated in Fig. 3D, driven by the dynamic magnetic field coupled with the optical field, the ferrofluid droplet ascends while executing a kayaking maneuver (movie S4). Programmable adjustments to the dynamic magnetic field allow for vertical uplift while performing rotational, tumbling, and stretching motions (see fig. S9 and movie S4). By periodically switching the light field on and off, ferrofluid droplets can rise and fall cyclically (Fig. 3, E and F). However, the maximum height reached by the ferrofluid droplet under the dynamic magnetic field is greater. This is attributed to the droplet continually changing shape under the dynamic magnetic field, which reduces heat generation from photothermal conversion and promotes liquid convection, resulting in lower droplet temperatures compared to those under static rising conditions.

Furthermore, by decreasing the light intensity and directing it onto one side of the droplet, we can induce controlled 2D motion of the droplet. This reduction in light intensity prevents the expansion of bubbles inside the droplet from generating enough force to counteract gravity, inhibiting upward floating motion. Simultaneously, irradiation on one side of the droplet governs the direction of the Marangoni flow, thereby dictating the droplet's motion. When the light field is illuminated at one end of the ferrofluid droplet, the induced internal Marangoni flow can propel the droplet to move horizontally within the horizontal plane (fig. S10). In addition, as demonstrated in fig. S11, the light field can selectively drive one of three ferrofluid droplets to move or manipulate all three droplets to fuse (movie S5). The speed of motion of the ferrofluid droplet in the 2D plane is correlated with the power of the external light field, with higher power resulting in increased motion speed (fig. S12). Overall, the light field can govern the movement of droplets along predetermined trajectories, including traversing slopes (fig. S13 and movie S5). Furthermore, the combined driving of optical and magnetic fields can confer more properties upon the droplets. For instance, controlled splitting of droplets can be achieved initially with a magnetic field, followed by selectively driving sub-droplets toward different target positions using the optical field (fig. S14 and movie S5).

Fission and assembly mechanism of droplet collectives

We further investigate the behavior of splitting and assembling of the droplets. The motion of an incompressible, immiscible ferrofluid droplet in an incompressible, immiscible medium under the effect of a uniform magnetic field is governed by the following continuity and momentum equations (*31*, *52*–*54*):

$$\nabla \cdot \mathbf{u} = 0 \tag{1}$$

$$\rho \frac{\mathrm{Du}}{\mathrm{Dt}} = -\nabla p + \nabla \cdot \tau + F_\sigma + F_m \tag{2}$$

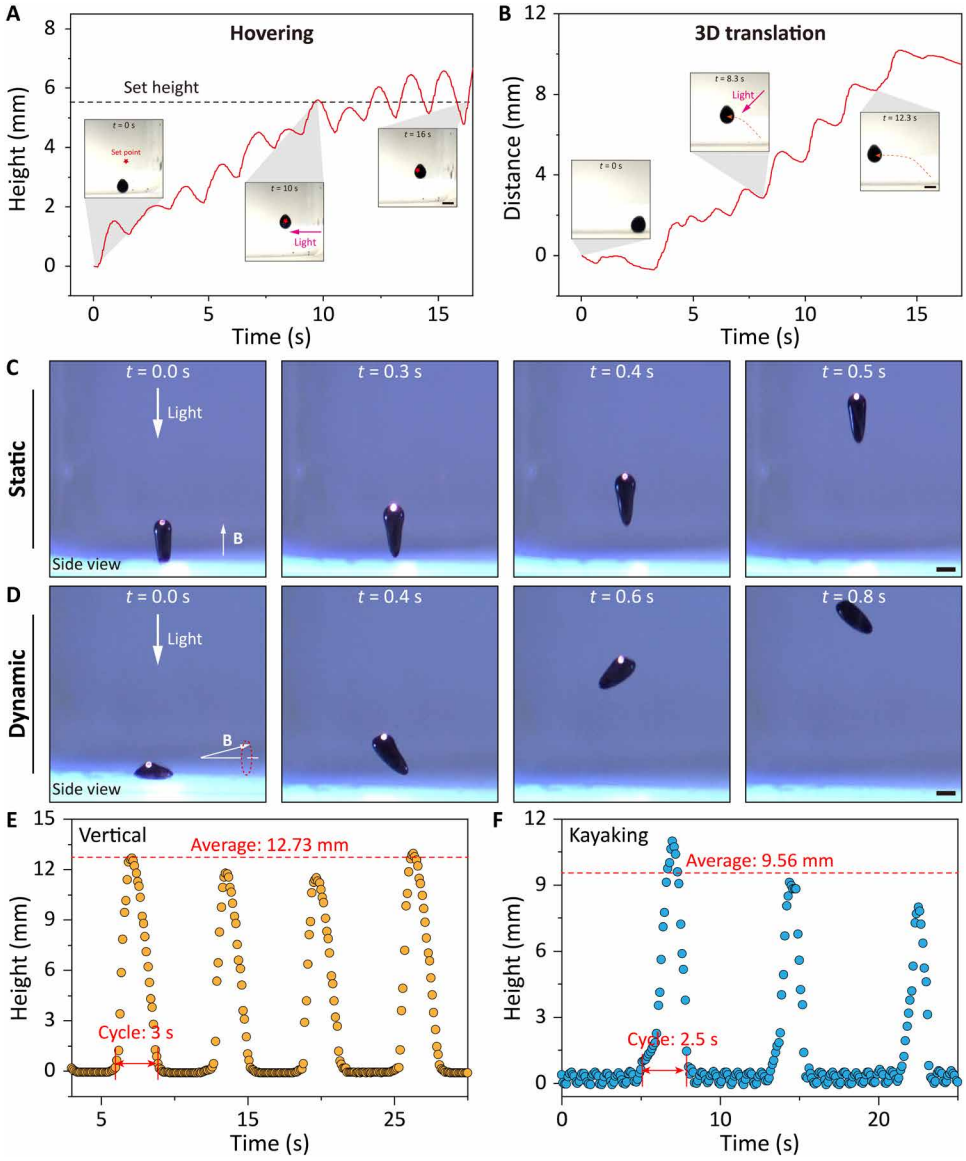

Fig. 3. Individual droplet movement behavior and control in 3D. (**A**) Height versus time of suspension of droplets under NIR irradiation (optical field, $I = 24$ W/cm^2; $D = 0°$ horizontal; magnetic field, off). The inset shows the suspension of a droplet under NIR irradiation. (**B**) Distance versus time for directional motion of a droplet under NIR irradiation (optical field, $I = 24$ W/cm^2; $D = 45°$ inclined; magnetic field, off). The inset shows the directional movement of a droplet under NIR irradiation. (**C**) Posture of droplets in 3D motion under static magnetic fields (optical field, $I = 24$ W/cm^2; $D = 90°$ vertical; magnetic field, $B = 9$ mT, $\alpha = 90°$). (**D**) Posture of droplets in 3D motion under dynamic magnetic fields (optical field, $I = 24$ W/cm^2; $D = 90°$ vertical; magnetic field, $B = 9$ mT, $f = 1$ Hz). (**E**) Height change of a liquid droplet during four cycles of motion under a static magnetic field (optical field, $I = 24$ W/cm^2; $D = 90°$ vertical; magnetic field, $B = 9$ mT, $\alpha = 90°$). (**F**) Height change of a liquid droplet during four cycles of motion under a dynamic magnetic field (optical field, $I = 24$ W/cm^2; $D = 90°$ vertical; magnetic field, $B = 9$ mT, $f = 1$ Hz). Scale bars, 3 mm.

where $\frac{\mathrm{Du}}{\mathrm{Dt}}$ represents the total derivative of the velocity field, $\mathbf{u}$. The right-hand side of the equation represents the force terms due to pressure, viscosity, surface tension (F_σ) and magnetic field (F_m) respectively. When subjected to a uniform oscillating magnetic field, the droplet undergoes splitting. To analyze this phenomenon effectively, we introduce dimensionless groups to reduce the number of variables and identify which dimensionless groups have the most substantial impact on droplet dynamics. The dimensionless groups are defined as (*53*, *54*):

$$Re = \frac{\rho_c R_0^2 \dot{\gamma}}{\eta_c} \tag{3}$$

$$Ca = \frac{\eta_c R_0 \dot{\gamma}}{\sigma} \tag{4}$$

$$Bo_m = \frac{R_0 \mu_0 H_0^2}{2\sigma} \tag{5}$$

where Re, Ca, and Bo_m represent the Reynolds, capillary, and magnetic bond numbers, respectively. As shown in Fig. 4A, the COMSOL simulation reproduces the splitting process of the droplet. The distribution of the flow field during droplet splitting is shown in fig. S15. In addition, we have investigated the dynamic behavior of droplets at different oscillating frequencies (fig. S16).

The split sub-droplets can be assembled into collective structures with different modes under different magnetic fields settings. The assembly behavior of droplets is mainly dominated by magnetic and fluid forces, which can be expressed as follows (*31*):

$$\sum_{\alpha=1,\beta\neq\alpha}^{N}\{\mathbf{F}^{m}_{\alpha,\beta}+\mathbf{F}^{t}_{\alpha,\beta}+\mathbf{F}^{r}_{\alpha,\beta}\}+\mathbf{F}^{n}=\mathbf{F}^{d}=6\pi\eta a(\mathbf{v}-\mathbf{v}_0) \quad (6)$$

where $\mathbf{F}^{m}_{\alpha,\beta}$ is the magnetic dipole force, $\mathbf{F}^{t}_{\alpha,\beta}$ is the hydrodynamic thrust force, $\mathbf{F}^{r}_{\alpha,\beta}$ is the repulsive force, $\mathbf{F}^{n}$ is the net force of gravity, and $\mathbf{F}^{d}$ is the drag force. The droplet assembly process under different oscillating magnetic field parameters is reproduced by simulation (Fig. 4B). The oscillating magnetic field is defined as:

$$\mathbf{B}_{v}=\begin{bmatrix}A_O\sin(2\pi ft)\cos\theta+C_O\sin\theta\\0\\A_O\sin(2\pi ft)\sin\theta+C_O\cos\theta\end{bmatrix} \quad (7)$$

where A_O is the amplitude of the sinusoidal signal, C_O is the intensity of the constant component, and θ is the direction angle. The amplitude ratio ($\lambda = A_O/C_O$) is proposed. When the parameter λ is 1, the sub-droplets generated after splitting will assemble to form a

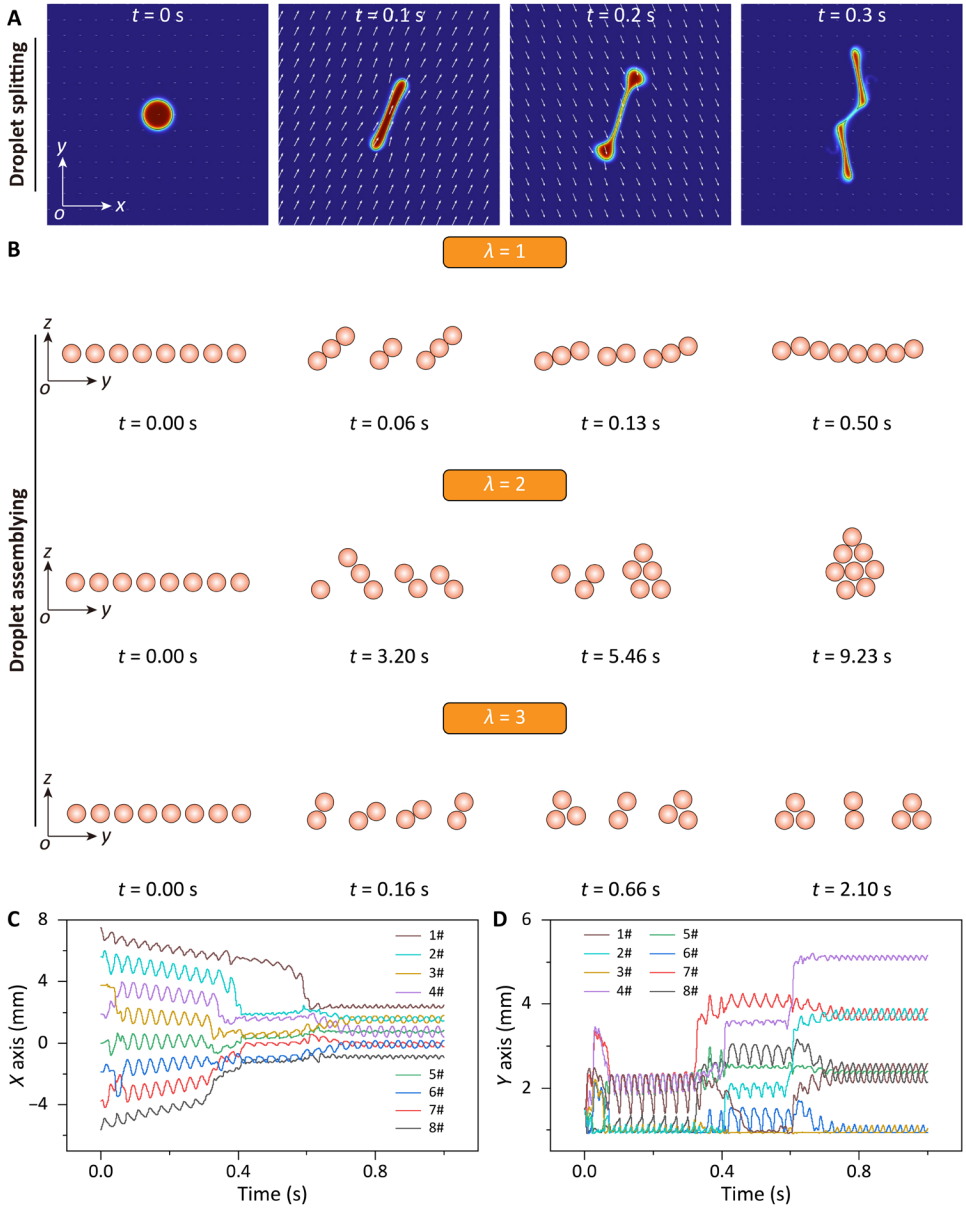

Fig. 4. Simulation of droplet splitting and assembly. (**A**) Simulation reproduces the splitting of a droplet into two under an oscillating magnetic field. (**B**) Droplets aggregated to form different collectives under different magnetic field parameters. (**C**) *X* coordinate of the eight droplets during assembly versus time (λ = 2). (**D**) *Y* coordinate of the eight droplets during assembly versus time (λ = 2).

chain-like structure; when λ is 2, the sub-droplets generated by splitting will assemble to form a layer-stacked structure; and when λ is 3, the sub-droplets generated by splitting will assemble to form an independent column-like structure. During the assembly process, the motion trajectories of sub-droplets inside layer-stacked structure are shown in Fig. 4 (C and D). The trajectories of the particles indicate that there is positional interchange behavior between the particles during the assembly process, and the spacing gradually becomes smaller along the *X* direction and larger along the *Y* direction, finally reaching a stable equilibrium state. The particle trajectory for the cases of $\lambda = 1$ and $\lambda = 3$ are shown in figs. S17 and S18, respectively.

Manipulation of droplet collectives

Droplets exhibit the ability to split and subsequently self-assemble under a predefined magnetic field into collective formations, manifesting in various modes such as chains, layer-by-layer assemblies, and columns. However, these droplet collectives typically rely on the substrate for assembly and movement under a separate magnetic field (*31*, *35*, *36*). The introduction of an optical field provides the droplet collectives with greater degrees of freedom, enhancing their capabilities. Like individual magnetic fluid droplets, the formed collectives can achieve levitation behavior. For instance, in Fig. 5A, under an oscillating magnetic field (with $\lambda = 1$), the sub-droplets form chain-like collectives (movie S6). Under side light field irradiation, the entire chain-like collectives can remain stable without further splitting and float upward in motion. Upon turning off the light field, the chain-like collectives descend. Similarly, by adjusting the magnetic field, droplet collectives can form a layered structure (with $\lambda = 2$), and these layer-assembled droplet collectives can be suspended under side light field irradiation (as depicted in Fig. 5B and movie S6). Simulation results depict the entire uplift of the droplet collectives and the trajectories of the particles (refer to figs. S19 and S20). Furthermore, in Fig. 5C, when driven by a separate magnetic field, ferrofluid droplets can first split and then assemble into a columnar structure (with $\lambda = 3$). The maximum height of the columnar structure is limited to four layers of the sub-droplet thickness h_1 (movie S7). This limitation arises because of the magnetic repulsion force preventing further assembly of the columnar structure. Subsequently, a light field is applied to induce translational movement of the basic columnar structure without interfering with other columns. The irradiated column then assembles and eventually reaches a height of h_2, which is 2.5 times higher than h_1. In addition, dispersed sub-droplets can be individually manipulated by the light field and assembled into desired patterns, such as triangles and the word "Ferrofluid" (fig. S21).

Potential application demonstration of the droplet

While droplet robots propelled by a 3D magnetic field face limitations in selectively driving multiple droplet robots within the same space due to the global nature of the magnetic field itself, as previously discussed (*46*, *47*), the proposed bimodal actuation strategy overcomes this challenge. Illustrated in Fig. 6A, this strategy facilitates the sequential splitting of droplets into two sub-droplets through cooperative action of magnetic and light fields, enabling object delivery tasks in both 2D and 3D spaces (movie S8). Initially positioned at the start of an artificially constructed labyrinth at $t = 0.0$ s, the droplet traverses to the intermediate region driven by a magnetic field within 40.6 s. Subsequently, another oscillating magnetic field is applied to induce controlled splitting of the droplet into two sub-droplets. These sub-droplets are then individually driven by a light field to traverse a vertical wall and reach the target position at $t = 180.0$ s. Notably, the droplet on the right, guided by the vertical light field, transports a flake to the surface at $t = 240.0$ s, while the droplet on the left, influenced by a magnetic field, carries a spherical object from one end to the other. The bimodal driving strategy significantly enhances the droplet robot's versatility, expanding its functionality by orchestrating multiple droplets in tandem to accomplish diverse tasks sequentially.

In addition to functioning autonomously and accomplishing various tasks as a liquid robot, droplets can also serve as actuators when combined with other components to assemble a soft robot. Leveraging the remarkable photothermal conversion ability of ferrofluid droplets, they can generate thermobuoyant flow under a light field, enabling 3D motion not only for a single droplet but also for the entire droplet assembly. As depicted in Fig. 6B, when assembled with a hydrogel, a jellyfish-shaped robot can be formed, capable of floating motion under NIR laser irradiation (movie S9). Initially positioned on the substrate at $t = 0.0$ s, the jellyfish robot rises vertically upward upon vertical light field irradiation, reaching the water surface at $t = 126.2$ s. Subsequently, driven by the light field, the jellyfish robot moves along the water surface at $t = 192.9$ s. Moreover, swarm motion of multiple jellyfish robots can be achieved by applying a horizontal light field, as illustrated in Fig. 6C. Under the illumination of a horizontal light field, three jellyfish robots rise sequentially to form a robot swarm (movie S9). Droplets exhibit excellent photothermal conversion efficiency, enabling the powering of jellyfish robot assembly with sunlight to facilitate 3D motion. As illustrated in Fig. 6D, sunlight is focused and vertically irradiated on the jellyfish robots using a magnifying glass, inducing the generation of fluids that cause them to float vertically (movie S9). By sequentially irradiating different jellyfish robots, all of them can achieve upward floating motion. The unique property of fluid droplets to assemble with other droplets or materials such as hydrogels substantially expands the capabilities of soft robots and greatly enlarges their design space.

DISCUSSION

In this study, we introduce a dual-modal driving strategy that synergistically integrates magnetic and optical fields to enable precise 3D motion and manipulation of individual ferrofluidic droplets as well as groups of droplets. These droplets, composed of an oil phase and iron tetraoxide, exhibit exceptional magnetic responsiveness and photothermal efficiency, rendering them highly conducive to controlled manipulation. The optical field serves as a key driver in inducing Marangoni flows around the droplets and triggering volume expansion, thereby enhancing their buoyancy. This combined effect propels both individual droplets and droplet collectives to move in 3D or regulate the morphology of droplet assemblies. In addition, the introduction of magnetic fields enables controlled splitting and assembly of droplets. By fine-tuning the magnetic field parameters, droplets can be precisely divided into multiple sub-droplets on demand. Subsequently, different droplets can be selectively driven by the light field to execute distinct tasks. Furthermore, magnetic field–driven droplets have the capacity to assemble into chain-like or layer-stacked structures, while the application of a light field confers upon these droplet collectives the ability to maneuver in 3D. The

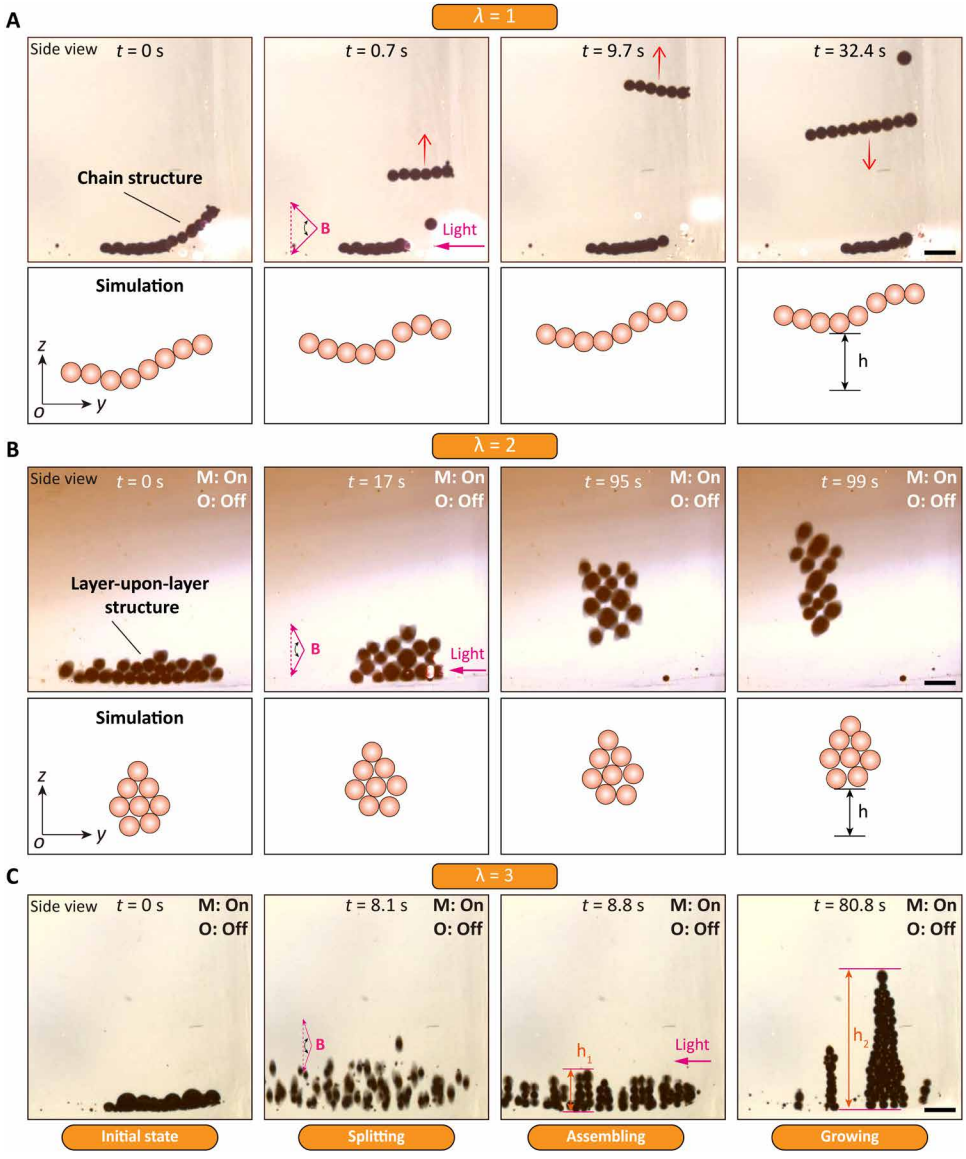

Fig. 5. Manipulating droplet collectives. (**A**) Droplets aggregate to form a chain-like structure, and the chain-like structure maintains overall uplift under the light field (optical field, $I = 36\ W/cm^2$; $D = 0°$ horizontal; magnetic field, $A_O = 9$ mT, $C_O = 9$ mT, $f = 25$ Hz). (**B**) Droplets aggregate to form a layer-upon-layer structure, and the structure maintains hovering under the light field (optical field, $I = 36\ W/cm^2$; $D = 0°$ horizontal; magnetic field, $A_O = 9$ mT, $C_O = 4.5$ mT, $f = 30$ Hz). (**C**) Ferrofluid droplets form a pyramidal structure (optical field, $I = 36\ W/cm^2$; $D = 0°$ horizontal; magnetic field, $A_O = 9$ mT, $C_O = 3$ mT, $f = 40$ Hz). Scale bars, 3 mm.

mechanism governing dual field–regulated droplet motion is elucidated and validated through comprehensive simulations, corroborating experimental observations. Even in various extreme environments, such as acidic and alkaline liquids, flowing liquids, different biofluids, and sticky glycerin, our proposed droplet 3D manipulation method is still feasible (figs. S22, S23, S24, and S25). These findings present an efficient strategy for droplet manipulation, broadening the capabilities of droplet-based robotics.

A notable challenge in magnetic control is the selective control of multiple untethered robots. Different from traditional robots, it is difficult to equip miniature soft robots with actuators and onboard sensors for motion and control. Therefore, independent control of multiple miniature robots is challenging as all magnetic robots receive the same control inputs in a single external field (*55*–*57*). Previously unidentified actuation strategies are desired to achieve selective control and expand the operating efficiency of magnetic robots. In the current work, we propose a feasible solution to combine the global magnetic field with the optical field, which has an adjustable operation region. We demonstrate the utilization of 3D moving droplets as droplet robots for cargo transportation or their integration with other modules to form soft robots capable of controlled movements driven by light fields. This approach represents a solid advancement in droplet manipulation, offering exciting prospects for the development of dynamic and adaptive miniature systems. Furthermore, within different formats of microrobots, liquid microrobots, particularly those structured as droplets, exhibit

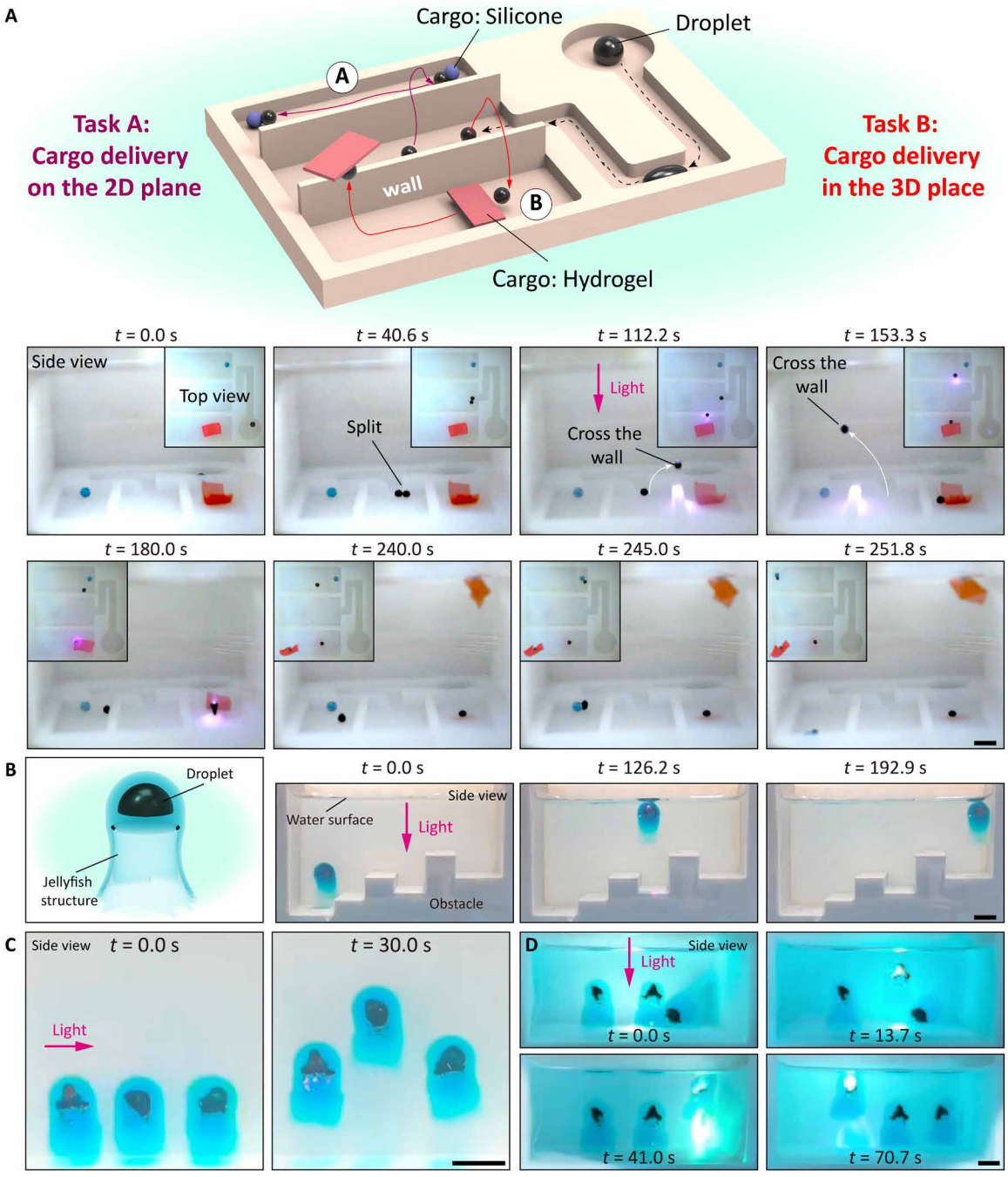

Fig. 6. Liquid droplets as soft robots. (**A**) Droplets as soft liquid robots can selectively perform transportation tasks (optical field, $I = 36$ W/cm^2; $D = 90°$ vertical; magnetic field, $A_O = 9$ mT, $C_O = 9$ mT, $f = 5$ Hz). (**B**) Droplet is assembled into jellyfish structures that flip through complex obstacles in a light field (optical field, $I = 48$ W/cm^2; $D = 90°$ vertical; magnetic field, off). (**C**) Multiple jellyfish-like robots move in groups (optical field, $I = 48$ W/cm^2; $D = 0°$ horizontal; magnetic field, off). (**D**) Jellyfish-like robot driven in sunlight (optical field, sunlight; $D = 90°$ vertical; magnetic field, off). Scale bars, 1 mm.

noteworthy attributes. Their fluidic composition endows them with an exceptional capacity to maneuver through constrictions significantly smaller than their original dimensions, thereby exemplifying a remarkable versatility in locomotion. In addition, the inherent fluidity of droplet microrobots offers substantial operational flexibility, facilitating actions such as the partitioning of a single droplet into multiple sub-droplets or the fusion of disparate sub-droplets into a unified entity. Such capabilities render droplet microrobots proficient in tasks ranging from cargo conveyance to micro-assembly, an advantageous trait particularly esteemed in the biochemical applications.

The droplet manipulation methods proposed in this article have several limitations. First, the application of droplet 3D manipulation

may be limited because of the limited penetration depth of the light field. Using a catheter to introduce the light source into deeper opaque regions is a viable strategy to extend optical actuation to more fields. Second, strong light fields induce intense temperature changes when driving droplets moving in three dimensions, which are unfavorable for applications such as bio-sample transportation and temperature-sensitive reactions. However, the temperature rise may be exploited for hyperthermia therapy. To avoid drastic temperature rises that could cause harm to the human body or biological samples, low-power density light fields should be used in these applications. Another potential improvement is to increase the initial bubble volume and decrease the density of the droplets so that they can lift under lower temperatures.

MATERIALS AND METHODS

Preparation of the ferrofluids and the hydrogel-ferrofluid composites

The fabrication process of oleic acid–coated Fe_3O_4 nanoparticles involved several steps. Initially, solutions of $FeCl_3$ (1.2 g/ml) and $FeCl_2$ (1.3 g/ml) were prepared, mixed in a beaker, and mechanically stirred for 20 min. The solution was then heated in an 80°C water bath. Concentrated ammonia was subsequently added dropwise until the pH reached 10, followed by continued reaction for 35 min. Next, a mixture of 4 g of oleic acid and 20 ml of ammonia was added to the reaction beaker and stirred for an additional 40 min. Dilute hydrochloric acid was then added dropwise until the pH was adjusted to 7. After allowing the solution to precipitate completely, it was discarded, and the precipitate was washed three to five times with anhydrous ethanol. The resulting precipitate was dried in a vacuum oven, ground, and stored in brown glass bottles. This powder was further washed with anhydrous ethanol, dried, mixed with an appropriate amount of corn oil, ground, and stirred. After standing for 24 hours, the supernatant obtained constituted the desired oil-based ferrofluid. Notably, the ferrofluids we produce are not indispensable for the optical response; we have conducted tests on commercial ferrofluids (EMG 905, FerroTec), which also exhibit behaviors akin to ours (fig. S27). This similarity arises from the fact that the optical response of the droplets primarily hinges on their main constituent, iron tetraoxide nanoparticles, which have light-absorbing properties, particularly in the NIR spectrum, and convert this absorbed energy into thermal energy. To enhance optical responsiveness, it is preferable to select a driving light source with wavelengths typically falling between 790 and 2526 nm.

To build the jellyfish-like robots, hydrogel-ferrofluid composites were fabricated via a mold-casting method (fig. S28). First, molds A and B were prepared with 3D-printed polylactide material. A hydrogel precursor comprising acrylamide, *N*,*N*′-methylenebisacrylamide, ammonium persulfate, *N*,*N*,*N*′,*N*′-tetramethylethane-1,2-diamine, and deionized water (10:0.1:0.1:0.01:89.79 in wt%, chemicals purchased from Sigma-Aldrich without any modification) was injected into the dome-shaped cavity between mold A and B. After curing, the dome-shaped hydrogel was carefully demolded and put into mold C leaving the opening toward the outside. Then, 10 μl of ferrofluid was injected into the cavity of the dome-like hydrogel, and another hydrogel precursor was injected into the mold to seal the ferrofluid droplet in the hydrogel. During injection, a magnet is used to keep the location of the ferrofluid droplet.

Setup for experiments

A setup comprising three orthogonal pairs of custom-made electromagnets was used, with an internal chamber size of 50 mm by 50 mm by 50 mm. Software-controlled signals dictated the input currents driving the electromagnets through a custom electronic board, enabling adjustable magnetic field intensities ranging from off to a maximum of 9 mT. The light source used in the study was an 808-nm NIR light from Hi-Tech Optoelectronics (LOS-BLD-0808-15 W-C/P), offering adjustable optical field power levels from 0 to 15 W. A 3D printer (Pro2, RAISE3D) was used to construct various terrains, including gaps, walls, and channels, used in the experimental setup. High-speed camera observations were conducted using an M310 camera from Phantom Inc. to analyze the motion behavior of the droplets.

Thermal characterization of the ferrofluid droplets

The temperature of the ferrofluid droplet under varying light field intensities was measured using an infrared camera (ETS320, Teledyne FLIR). To ensure accurate positioning, the ferrofluid droplet was visually centered in the tank at the desired height, with permanent magnets placed beneath the tank to stabilize the droplets. Given the fixed focus distance of 7 cm for the infrared camera, it was positioned 7 cm above the ferrofluid droplet during the experiments. Before testing, the camera underwent calibration using reference points: melting ice and boiling water. For the experiments, 10 μl of ferrofluid was meticulously introduced into the same container under both empty and water-filled conditions. Subsequently, the temperature variations of the ferrofluid droplets, subjected to continuous light field input, were recorded and analyzed.

Simulation of droplet splitting

Figure S29 illustrates a schematic representation of a ferrofluid droplet suspended in another fluid medium experiencing an oscillating magnetic field, $\boldsymbol{B}_v$ (*7*). In this scenario, the magnetic susceptibility of the ferrofluid droplet was assumed to be 2.65 (χ_d), while it was considered zero (χ_c) for the suspending nonmagnetic fluid. Subscripts *c* and *d* denote the continuous phase and droplet, respectively. The viscosity and density of both phases were assumed to be $\eta_c = 6$ cP, $\eta_d = 1$ cP, and $\rho_d = 1290$ kg/m^3, $\rho_c = 1000$ kg/m^3 individually. The dimensions of the computational domain were set to $H_{\text{domain}} = W_{\text{domain}} = 16\ R_0$, where R_0 represents the radius of the undeformed ferrofluid droplet. Initially, the ferrofluid droplet is positioned at the center of the computational domain. The surface tension of ferrofluid is considered as 13.5 mN/m, and surface tension of water is considered as 73 mN/m. This setup investigates the deformation of the droplet under the oscillating magnetic field.

A two-phase laminar flow model using the level set method, combined with transient simulation and phase initialization, was used to simulate the flow domain and track the deformable interface of the droplet. The level set function, denoted as Φ, is assigned values of 1 and 0 for the droplet phase and continuous phase, respectively, to define the interface of the droplet using initial interface conditions. The reinitialization parameter, γ was set equal to the maximum magnitude of the velocity in the flow domain, and the interface thickness, ε was chosen to be of the same order as the size of the mesh elements. In addition, a magnetic field was applied to the flow domain and solved simultaneously using the magnetic fields and no currents interface from AC/DC module. In this case, the magnetic field was applied in 2D plane, and magnetic insulation

was applied to both left and right walls. The time-dependent solver is used for analyzing droplet deformation under the varying magnetic field frequency 0.5 to 10 Hz. The mesh was created using free triangular elements in the computational domain, and the PARDISO solver with nested dissection multithread algorithm is used to solve the computational model.

Simulation of droplet floating due to light irradiation

A two-phase laminar flow model using the level set method, combined with transient simulation and phase initialization, was used to simulate the flow domain. A Marangoni effect module was applied to the boundary of two phases to couple the flow field with heat transfer, where the surface tension coefficient was set as default from the materials library. A heat source was applied to the ferrofluid phase with equation $q_0 = 10^{8*}\Phi[Wm^{-3}]$, where $\Phi = 1$ for the ferrofluid phase and $\Phi = 0$ for the nonmagnetic phase. Droplet splitting and floating were simulated by COMSOL Multiphysics software.

Simulation of droplet assembling

On the basis of Eq. 6, we conducted simulations to investigate the motion behavior of colloidal particles. Our custom interface programmed with MATLAB software was used to study the assembling process of droplet collectives under the influence of an oscillating magnetic field. In our simulations, the droplet diameter was fixed at 1.5 mm, the colloid density was set to 1290 kg/m^3, and the magnetic susceptibility was set as 2.65. The strength of magnetic field was set as 9 mT, and the frequency was varied from 1 to 100 Hz. The parameters of droplet in the simulation are summarized in table S1.

Supplementary Materials

This PDF file includes:

Supplementary Note 1
Figs. S1 to S29
Table S1
Legends for movies S1 to S9

Other Supplementary Material for this manuscript includes the following:

Movies S1 to S9

REFERENCES AND NOTES

1. W. Li, L. Zhang, X. Ge, B. Xu, W. Zhang, L. Qu, C.-H. Choi, J. Xu, A. Zhang, H. Lee, D. A. Weitz, Microfluidic fabrication of microparticles for biomedical applications. *Chem. Soc. Rev.* **47**, 5646–5683 (2018).
2. Y. Wang, R. Jin, B. Shen, N. Li, H. Zhou, W. Wang, Y. Zhao, M. Huang, P. Fang, S. Wang, P. Mary, R. Wang, P. Ma, R. Li, Y. Tian, Y. Cao, F. Li, L. Schweizer, H. Zhang, High-throughput functional screening for next-generation cancer immunotherapy using droplet-based microfluidics. *Sci. Adv.* **7**, eabe3839 (2021).
3. A. C. Sun, D. J. Steyer, A. R. Allen, E. M. Payne, R. T. Kennedy, C. R. J. Stephenson, A droplet microfluidic platform for high-throughput photochemical reaction discovery. *Nat. Commun.* **11**, 6202 (2020).
4. J. Li, Y. Hou, Y. Liu, C. Hao, M. Li, M. K. Chaudhury, S. Yao, Z. Wang, Directional transport of high-temperature Janus droplets mediated by structural topography. *Nat. Phys.* **12**, 606–612 (2016).
5. M. Damak, K. K. Varanasi, Electrostatically driven fog collection using space charge injection. *Sci. Adv.* **4**, eaao5323 (2018).
6. R. A. Hayes, B. J. Feenstra, Video-speed electronic paper based on electrowetting. *Nature* **425**, 383–385 (2003).
7. W. Lei, G. Hou, M. Liu, Q. Rong, Y. Xu, Y. Tian, L. Jiang, High-speed transport of liquid droplets in magnetic tubular microactuators. *Sci. Adv.* **4**, eaau8767 (2018).
8. A. Li, H. Li, Z. Li, Z. Zhao, K. Li, M. Li, Y. Song, Programmable droplet manipulation by a magnetic-actuated robot. *Sci. Adv.* **6**, eaay5808 (2020).
9. J. Li, N. S. Ha, T. L. Liu, R. M. van Dam, C. J. Kim, Ionic-surfactant-mediated electrodewetting for digital microfluidics. *Nature* **572**, 507–510 (2019).
10. Y. Jin, W. Xu, H. Zhang, R. Li, J. Sun, S. Yang, M. Liu, H. Mao, Z. Wang, Electrostatic tweezer for droplet manipulation. *Proc. Natl. Acad. Sci. U.S.A.* **119**, e2105459119 (2022).
11. J. Lv, Y. Liu, J. Wei, E. Chen, L. Qin, Y. Yu, Photocontrol of fluid slugs in liquid crystal polymer microactuators. *Nature* **537**, 179–184 (2016).
12. W. Li, X. Tang, L. Wang, Photopyroelectric microfluidics. *Sci. Adv.* **6**, eabc1693 (2020).
13. S. P. Zhang, J. Lata, C. Chen, J. Mai, F. Guo, Z. Tian, L. Ren, Z. Mao, P.-H. Huang, P. Li, S. Yang, T. J. Huang, Digital acoustofluidics enables contactless and programmable liquid handling. *Nat. Commun.* **9**, 2928 (2018).
14. Z. Yuan, C. Lu, C. Liu, X. Bai, L. Zhao, S. Feng, Y. Liu, Ultrasonic tweezer for multifunctional droplet manipulation. *Sci. Adv.* **9**, eadg2352 (2023).
15. J. V. I. Timonen, M. Latikka, L. Leibler, R. H. A. Ras, O. Ikkala, Switchable static and dynamic self-assembly of magnetic droplets on superhydrophobic surfaces. *Science* **341**, 253–257 (2013).
16. M. J. Fuerstman, P. Garstecki, G. M. Whitesides, Coding/decoding and reversibility of droplet trains in microfluidic networks. *Science* **315**, 828–832 (2007).
17. K. C. Park, P. Kim, A. Grinthal, N. He, D. Fox, J. C. Weaver, J. Aizenberg, Condensation on slippery asymmetric bumps. *Nature* **531**, 78–82 (2016).
18. Z. Ren, M. Sitti, Design and build of small-scale magnetic soft-bodied robots with multimodal locomotion. *Nat. Protoc.* **19**, 441–486 (2024).
19. Q. Wang, N. Xiang, J. Lang, B. Wang, D. Jin, L. Zhang, Reconfigurable liquid-bodied miniature machines: Magnetic control and microrobotic applications. *Adv. Intell. Syst.* **6**, 2300108 (2023).
20. M. Sitti, Miniature soft robots-road to the clinic. *Nat. Rev. Mater.* **3**, 74–75 (2018).
21. M. Cianchetti, C. Laschi, A. Menciassi, P. Dario, Biomedical applications of soft robotics. *Nat. Rev. Mater.* **3**, 143–153 (2018).
22. M. Sitti, H. Ceylan, W. Hu, J. Giltinan, M. Turan, S. Yim, E. Diller, Biomedical applications of untethered mobile milli/microrobots. *Proc. IEEE* **103**, 205–224 (2015).
23. W. Hu, G. Z. Lum, M. Mastrangeli, M. Sitti, Small-scale soft-bodied robot with multimodal locomotion. *Nature* **554**, 81–85 (2018).
24. Y. Kim, H. Yuk, R. Zhao, S. A. Chester, X. Zhao, Printing ferromagnetic domains for untethered fast-transforming soft materials. *Nature* **558**, 274–279 (2018).
25. Y. Dong, L. Wang, N. Xia, Z. Yang, C. Zhang, C. Pan, D. Jin, J. Zhang, C. Majidi, L. Zhang, Untethered small-scale magnetic soft robot with programmable magnetization and integrated multifunctional modules. *Sci. Adv.* **8**, eabn8932 (2022).
26. N. Xia, D. Jin, C. Pan, J. Zhang, Z. Yang, L. Su, J. Zhao, L. Wang, L. Zhang, Dynamic morphological transformations in soft architected materials via buckling instability encoded heterogeneous magnetization. *Nat. Commun.* **13**, 7514 (2022).
27. S. Chen, H.-Z. Wang, R.-Q. Zhao, W. Rao, J. Liu, Liquid metal composites. *Matter* **2**, 1446–1480 (2020).
28. Y. Shen, D. Jin, M. Fu, S. Liu, Z. Xu, Q. Cao, B. Wang, G. Li, W. Chen, S. Liu, X. Ma, Reactive wetting enabled anchoring of non-wettable iron oxide in liquid metal for miniature soft robot. *Nat. Commun.* **14**, 6276 (2023).
29. H. Wang, S. Chen, B. Yuan, J. Liu, X. Sun, Liquid metal transformable machines. *Acc. Mater. Res.* **2**, 1227–1238 (2021).
30. Q. Wang, C. Pan, Y. Zhang, L. Peng, Z. Chen, C. Majidi, L. Jiang, Magnetoactive liquid-solid phase transitional matter. *Matter* **6**, 855–872 (2023).
31. M. Sun, S. Yang, J. Jiang, L. Zhang, Horizontal and vertical coalescent microrobotic collectives using ferrofluid droplets. *Adv. Mater.* **35**, e2300521 (2023).
32. X. Fan, X. Dong, A. C. Karacakol, H. Xie, M. Sitti, Reconfigurable multifunctional ferrofluid droplet robots. *Proc. Natl. Acad. Sci. U.S.A.* **117**, 27916–27926 (2020).
33. M. Sun, B. Hao, S. Yang, X. Wang, C. Majidi, L. Zhang, Exploiting ferrofluidic wetting for miniature soft machines. *Nat. Commun.* **13**, 7919 (2022).
34. X. Fan, Y. Jiang, M. Li, Y. Zhang, C. Tian, L. Mao, H. Xie, L. Sun, Z. Yang, M. Sitti, Scale-reconfigurable miniature ferrofluidic robots for negotiating sharply variable spaces. *Sci. Adv.* **8**, eabq1677 (2022).
35. W. Yu, H. Lin, Y. Wang, X. He, N. Chen, K. Sun, D. Lo, B. Cheng, C. Yeung, J. Tan, D. di Carlo, S. Emaminejad, A ferrobotic system for automated microfluidic logistics. *Sci. Robot.* **5**, eaba4411 (2020).
36. H. Lin, W. Yu, K. A. Sabet, M. Bogumil, Y. Zhao, J. Hambalek, S. Lin, S. Chandrasekaran, O. Garner, D. di Carlo, S. Emaminejad, Ferrobotic swarms enable accessible and adaptable automated viral testing. *Nature* **611**, 570–577 (2022).
37. M. Sun, C. Tian, L. Mao, X. Meng, X. Shen, B. Hao, X. Wang, H. Xie, L. Zhang, Reconfigurable magnetic slime robot: Deformation, adaptability, and multifunction. *Adv. Funct. Mater.* **32**, 2112508 (2022).
38. A. Chiolerio, M. B. Quadrelli, Smart fluid systems: The advent of autonomous liquid robotics. *Adv. Sci.* **4**, 1700036 (2017).
39. L. Sun, F. Bian, Y. Wang, Y. Wang, X. Zhang, Y. Zhao, Bioinspired programmable wettability arrays for droplets manipulation. *Proc. Natl. Acad. Sci. U.S.A.* **117**, 4527–4532 (2020).
40. A. F. Demirörs, S. Aykut, S. Ganzeboom, Y. A. Meier, E. Poloni, Programmable droplet manipulation and wetting with soft magnetic carpets. *Proc. Natl. Acad. Sci. U.S.A.* **118**, e2111291118 (2021).

41. X. Zhang, L. Sun, Y. Wang, F. Bian, Y. Wang, Y. Zhao, Multibioinspired slippery surfaces with wettable bump arrays for droplets pumping. *Proc. Natl. Acad. Sci. U.S.A.* **116**, 20863–20868 (2019).
42. D. Chen, Z. Yang, Y. Ji, Y. Dai, L. Feng, F. Arai, Deformable ferrofluid-based millirobot with high motion accuracy and high output force. *Appl. Phys. Lett.* **118**, 134101 (2021).
43. R. Ahmed, M. Ilami, J. Bant, B. Beigzadeh, H. Marvi, A shapeshifting ferrofluidic robot. *Soft Robot.* **8**, 687–698 (2021).
44. X. Jing, H. Chen, L. Zhang, S. Zhao, Y. Wang, Z. Wang, Y. Zhou, Accurate magneto-driven multi-dimensional droplet manipulation. *Adv. Funct. Mater.* **33**, 2210883 (2023).
45. A. W. Zhou, C. Y. Xu, P. Kanitthamniyom, C. S. X. Ng, G. J. Lim, W. S. Lew, S. Vasoo, X. S. Zhang, G. Z. Lum, Y. Zhang, Magnetic soft millirobots 3D printed by circulating vat photopolymerization to manipulate droplets containing hazardous agents for in vitro diagnostics. *Adv. Mater.* **34**, e2200061 (2022).
46. R. Ahmed, R. Calandra, H. Marvi, Learning to control a three-dimensional ferrofluidic robot. *Soft Robot.* **11**, 218–229 (2024).
47. X. Fan, Y. Zhang, Z. Wu, H. Xie, L. Sun, T. Chen, Z. Yang, Combined three dimensional locomotion and deformation of functional ferrofluidic robots. *Nanoscale* **15**, 19499–19513 (2023).
48. M. Zhou, Z. Wu, Y. Zhao, Q. Yang, W. Ling, Y. Li, H. Xu, C. Wang, X. Huang, Droplets as carriers for flexible electronic devices. *Adv. Sci.* **6**, 1901862 (2019).
49. O. Oehlsen, S. I. Cervantes-Ramírez, P. Cervantes-Avilés, I. A. Medina-Velo, Approaches on ferrofluid synthesis and applications: Current status and future perspectives. *ACS Omega* **7**, 3134–3150 (2022).
50. M. Imran, A. R. Ansari, A. H. Shaik, S. Hussain, A. Khan, M. R. Chandan, Ferrofluid synthesis using oleic acid coated Fe_3O_4 nanoparticles dispersed in mineral oil for heat transfer applications. *Mater. Res. Express* **5**, 036108 (2018).
51. Y. Ji, X. Bai, H. Sun, L. Wang, C. Gan, L. Jia, J. Xu, W. Zhang, L. Wang, Y. Xu, Y. Hou, Y. Wang, H. Hui, L. Feng, Biocompatible ferrofluid-based millirobot for tumor photothermal therapy in near-infrared-II window. *Adv. Healthc. Mater.* **6**, e2302395 (2024).
52. L. H. Cunha, I. R. Siqueira, T. F. Oliveira, H. D. Ceniceros, Field-induced control of ferrofluid emulsion rheology and droplet break-up in shear flows. *Phys. Fluids* **30**, 122110 (2018).
53. M. R. Hassan, C. Wang, Magnetic field induced ferrofluid droplet breakup in a simple shear flow at a low Reynolds number. *Phys. Fluids* **31**, 127104 (2019).
54. M. R. Hassan, C. Wang, Ferro-hydrodynamic interactions between ferrofluid droplet pairs in simple shear flows. *Colloids. Surf. A Physicochem. Eng. Asp.* **602**, 124906 (2020).
55. E. Diller, J. Giltinan, M. Sitti, Independent control of multiple magnetic microrobots in three dimensions. *Int. J. Rob. Res.* **32**, 614–631 (2013).
56. E. Diller, S. Floyd, C. Pawashe, M. Sitti, Control of multiple heterogeneous magnetic microrobots in two dimensions on nonspecialized surfaces. *IEEE Trans. Robot.* **28**, 172–182 (2012).
57. T. Xu, C. Huang, Z. Lai, X. Wu, Independent control strategy of multiple magnetic flexible millirobots for position control and path following. *IEEE Trans. Robot.* **38**, 2875–2887 (2022).

Acknowledgments

Funding: This work was funded by the Max Planck Society, European Research Council (ERC) Advanced Grant SoMMoR project with grant no. 834531, German Research Foundation (DFG) Soft Material Robotic Systems (SPP 2100) Program with grant no. 2197/5-1, Research Impact Fund (project no. R4015-21), Research Fellow Scheme (project no. RFS2122-4S03), and Strategic Topics Grant (project no. STG1/E-401/23-N) from the Hong Kong Research Grants Council (RGC). We also thank the support from Multi-Scale Medical Robotics Centre (MRC), InnoHK, at the Hong Kong Science Park, and the SIAT-CUHK Joint Laboratory of Robotics. Mengmeng Sun thanks the Alexander von Humboldt Foundation for financial support. **Author contributions:** Mengmeng Sun, L.Z., and Metin Sitti conceived the idea and designed the research. Mengmeng Sun and B.S. carried out the experiments and analyzed the data with the help of S.Y., Y.W., M.Z., and W.K. M.P. conducted the simulation work. L.Z. and Metin Sitti supervised the research. Mengmeng Sun and B.S. wrote the manuscript with the input from all authors. All authors discussed the results and commented or edited on the manuscript. **Competing interests:** The authors declare that they have no competing interests. **Data and materials availability:** All data needed to evaluate the conclusions in the paper are present in the paper and/or the Supplementary Materials.

Submitted 11 March 2024
Accepted 14 June 2024
Published 17 July 2024
10.1126/sciadv.adp1439